ATLAS PUB Note

ATL-PHYS-PUB-2023-018

17th July 2023

Dark matter summary plots for *s*-channel, 2HDM+*a*, Higgs portal and Dark Higgs models

The ATLAS Collaboration

This note presents summary plots for dark matter simplified models with *s*-channel spin-1 and spin-0 mediators, a Two-Higgs-Doublet model with an extra pseudoscalar mediator (2HDM+*a*), Higgs portal models and a Dark Higgs model. Results shown are current as of July 2023.

1 Introduction

This document provides summary plots of mediator-based dark matter models, including s-channel models [1, 2], the 2HDM+a model [3], Higgs portal models [4, 5] and a Dark Higgs model [6] using results current as of July 2023. Results for s-channel models are discussed in Section 2. The 2HDM+a model is discussed in Section 3. The Higgs portal model is discussed in Section 4. The Dark Higgs model is discussed in Section 5.

2 s-channel summary plots

Simplified models of DM, introducing a single mediator that couples DM particles (usually modelled by a new Dirac fermion) to the SM particles were introduced [1, 2] at the beginning of Run-2 in order to circumvent the problems arising in the interpretation of EFT DM models. The mediator can be a scalar, pseudo-scalar, vector or axial-vector and the models contain four free parameters, namely the couplings of the mediator to the SM (g_q for quarks, g_ℓ for leptons) and DM particles (g_χ), as well as the mass of the mediator and the mass of the DM particles (m_χ).

A summary of the constraints on models with spin-1 (vector and axial-vector) mediators are presented in Section 2.1 and for spin-0 mediators (scalar and pseudo-scalar) are discussed in Section 2.2.

2.1 Spin-1 Mediators

Four benchmarks are considered for spin-1 mediators as follows:

Benchmark	g_χ	g_q	g_ℓ
Vector 1 (V1)	1	0.25	0
Vector 2 (V2)	1	0.1	0.01
Axial-vector 1 (AV1)	1	0.25	0
Axial-vector 2 (AV2)	1	0.1	0.1

The motivation for the specific choice of couplings is described in Ref. [7].

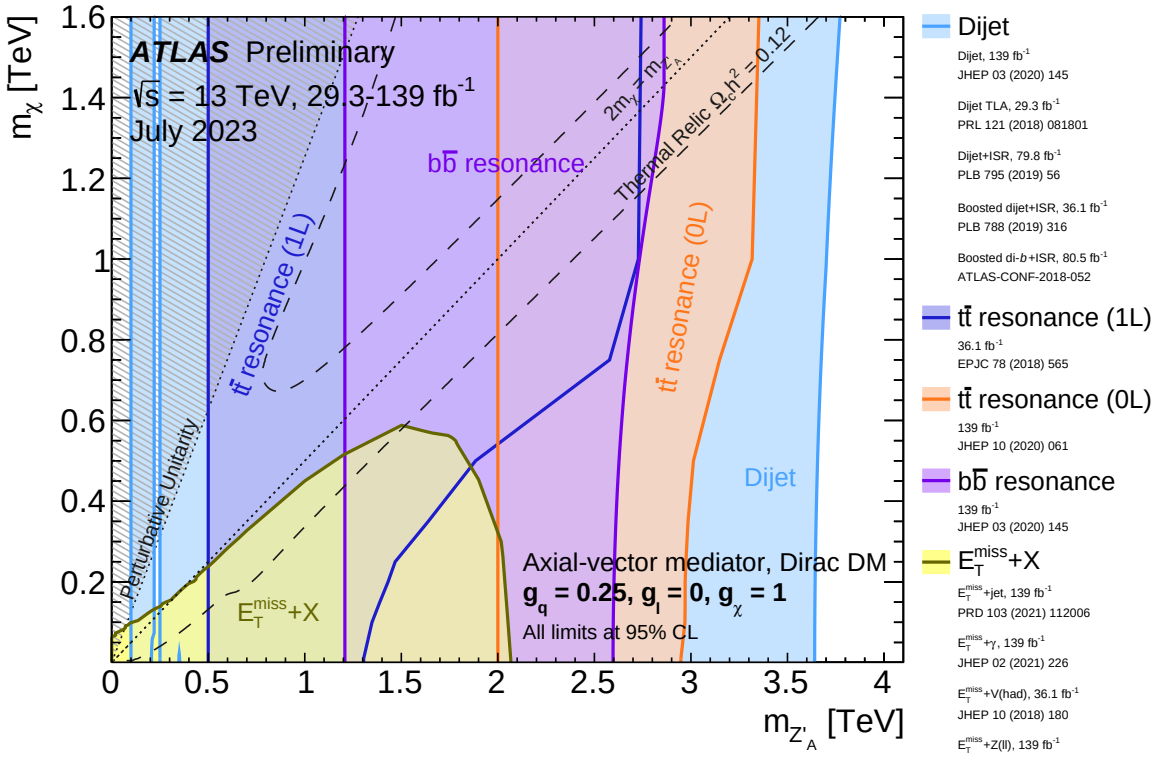

Figure 1: Regions in the (mediator-mass, DM-mass) plane excluded at 95% CL by visible and invisible searches, for leptophobic axial-vector mediator simplified models. Each shaded region represents the union of the exclusion contours of the individual analyses listed in the legend, where more than one result contributes. The exclusions are computed for a DM coupling $g_\chi = 1$, quark coupling $g_q = 0.25$, universal to all flavours, and no coupling to leptons. Dashed curves labelled "thermal relic" correspond to combinations of DM and mediator mass values that are consistent with a DM density of $\Omega h^2 = 0.12$ and a standard thermal history, as computed in MadDM [7, 8]. Between the two curves, annihilation processes described by the simplified model deplete Ωh^2 to below 0.12. A dotted line indicates the kinematic threshold where the mediator can decay on-shell into DM. Excluded regions that are in tension with the perturbative unitary considerations of Ref. [9] are indicated by shading in the upper left corner. The reinterpretation procedure for the TLA analysis follows the procedure recommended by ATLAS in Appendix A of Ref. [10], while the high-mass dijet and dijet+ISR analyses are reinterpreted following Ref. [11].

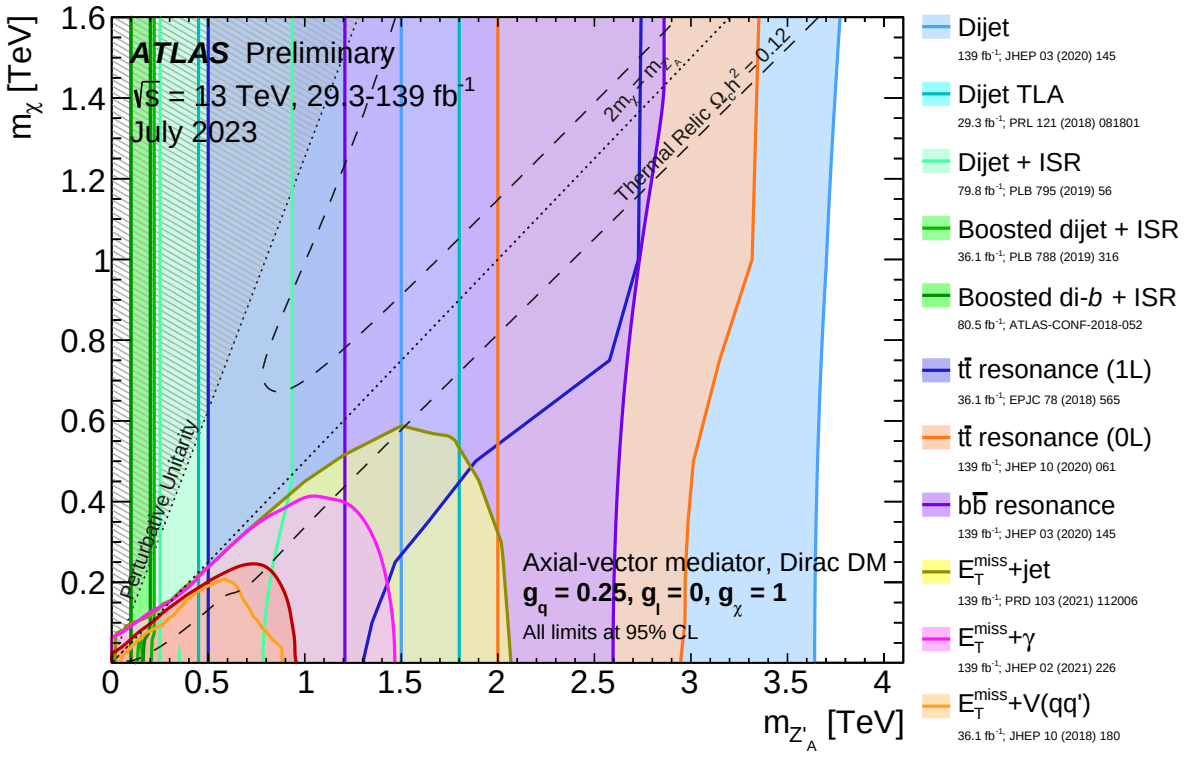

Figure 2: Regions in the (mediator-mass, DM-mass) plane excluded at 95% CL by visible and invisible searches, for leptophobic axial-vector mediator simplified models. The exclusions are computed for a DM coupling $g_\chi = 1$, quark coupling $g_q = 0.25$, universal to all flavours, and no coupling to leptons. Dashed curves labelled "thermal relic" correspond to combinations of DM and mediator mass values that are consistent with a DM density of $\Omega h^2 = 0.12$ and a standard thermal history, as computed in MadDM [7, 8]. Between the two curves, annihilation processes described by the simplified model deplete Ωh^2 to below 0.12. A dotted line indicates the kinematic threshold where the mediator can decay on-shell into DM. Excluded regions that are in tension with the perturbative unitary considerations of Ref. [9] are indicated by shading in the upper left corner. The reinterpretation procedure for the TLA analysis follows the procedure recommended by ATLAS in Appendix A of Ref. [10], while the high-mass dijet and dijet+ISR analyses are reinterpreted following Ref. [11].

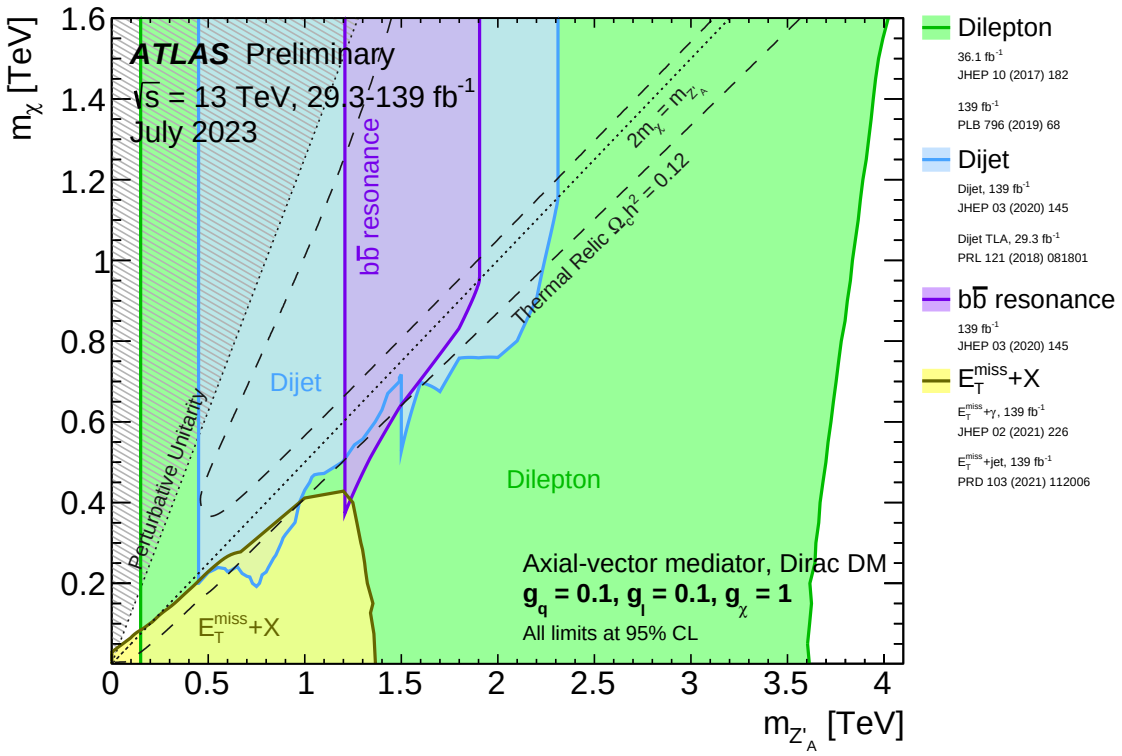

Figure 3: Regions in the (mediator-mass, DM-mass) plane excluded at 95% CL by visible and invisible searches, for leptophilic axial-vector mediator simplified models. Each shaded region represents the union of the exclusion contours of the individual analyses listed in the legend, where more than one result contributes. The exclusions are computed for a DM coupling $g_\chi = 1$, quark coupling $g_q = 0.1$, and lepton coupling $g_l = 0.1$, in both cases universal to all flavours. Dashed curves labelled "thermal relic" correspond to combinations of DM and mediator mass values that are consistent with a DM density of $\Omega h^2 = 0.12$ and a standard thermal history, as computed in MadDM [7, 8]. Between the two curves, annihilation processes described by the simplified model deplete Ωh^2 to below 0.12. A dotted line indicates the kinematic threshold where the mediator can decay on-shell into DM. Excluded regions that are in tension with the perturbative unitary considerations of Ref. [9] are indicated by shading in the upper left corner.

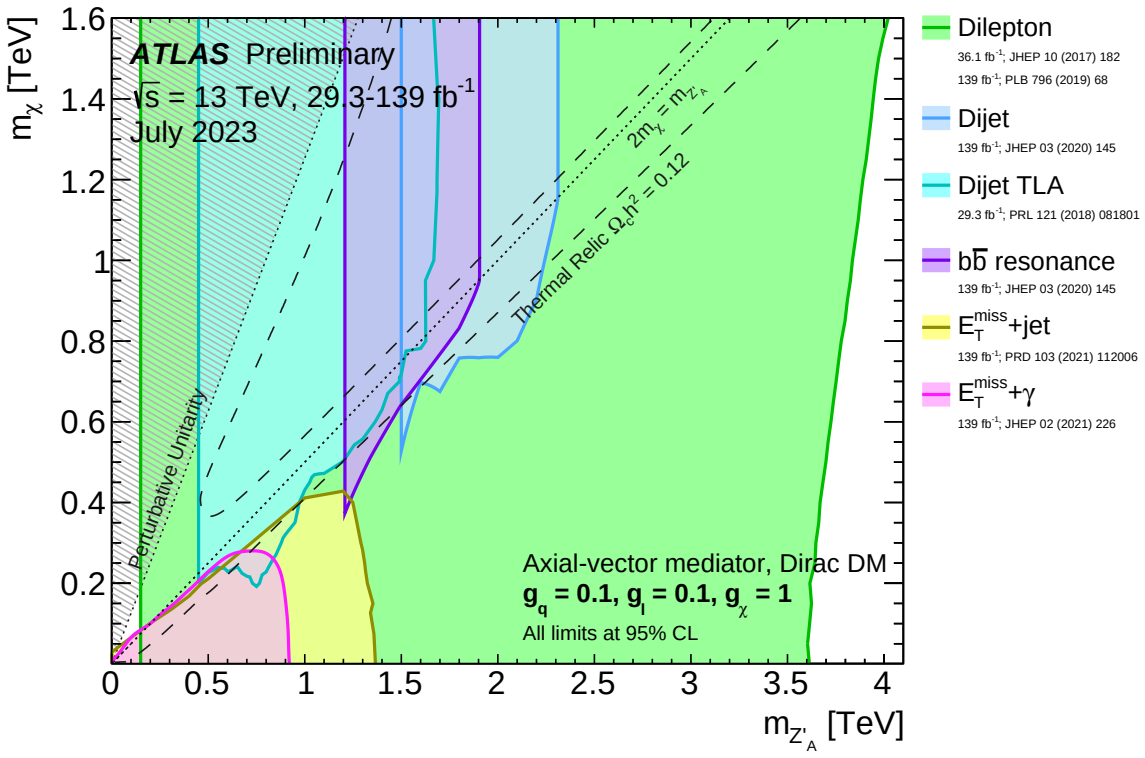

Figure 4: Regions in the (mediator-mass, DM-mass) plane excluded at 95% CL by visible and invisible searches, for leptophilic axial-vector mediator simplified models. The exclusions are computed for a DM coupling $g_\chi = 1$, quark coupling $g_q = 0.1$, and lepton coupling $g_l = 0.1$, in both cases universal to all flavours. Dashed curves labelled "thermal relic" correspond to combinations of DM and mediator mass values that are consistent with a DM density of $\Omega h^2 = 0.12$ and a standard thermal history, as computed in MadDM [7, 8]. Between the two curves, annihilation processes described by the simplified model deplete Ωh^2 to below 0.12. A dotted line indicates the kinematic threshold where the mediator can decay on-shell into DM. Excluded regions that are in tension with the perturbative unitary considerations of Ref. [9] are indicated by shading in the upper left corner.

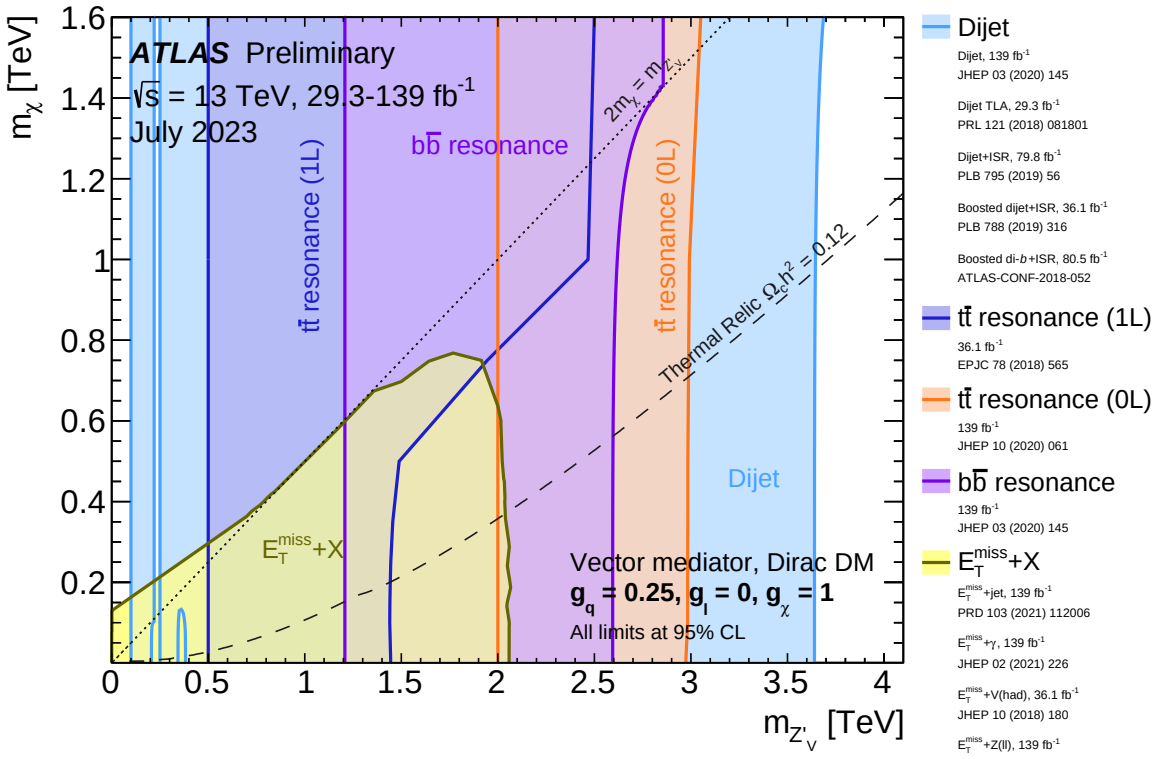

Figure 5: Regions in the (mediator-mass, DM-mass) plane excluded at 95% CL by dijet, dilepton and $E_{\mathrm{T}}^{\mathrm{miss}}+X$ searches, for leptophobic vector mediator simplified models. Each shaded region represents the union of the exclusion contours of the individual analyses listed in the legend, where more than one result contributes. The exclusions are computed for a DM coupling $g_\chi = 1$, quark coupling $g_q = 0.25$, universal to all flavours, and no coupling to leptons. Dashed curves labelled "thermal relic" correspond to combinations of DM and mediator mass values that are consistent with a DM density of $\Omega h^2 = 0.12$ and a standard thermal history as computed in MadDM [7, 8]. Above the curve, annihilation processes described by the simplified model deplete Ωh^2 to below 0.12. The dotted line indicates the kinematic threshold where the mediator can decay on-shell into DM. The reinterpretation procedure for the TLA analysis follows the procedure recommended by ATLAS in Appendix A of Ref. [10], while the high-mass dijet and dijet+ISR analyses are reinterpreted following Ref. [11].

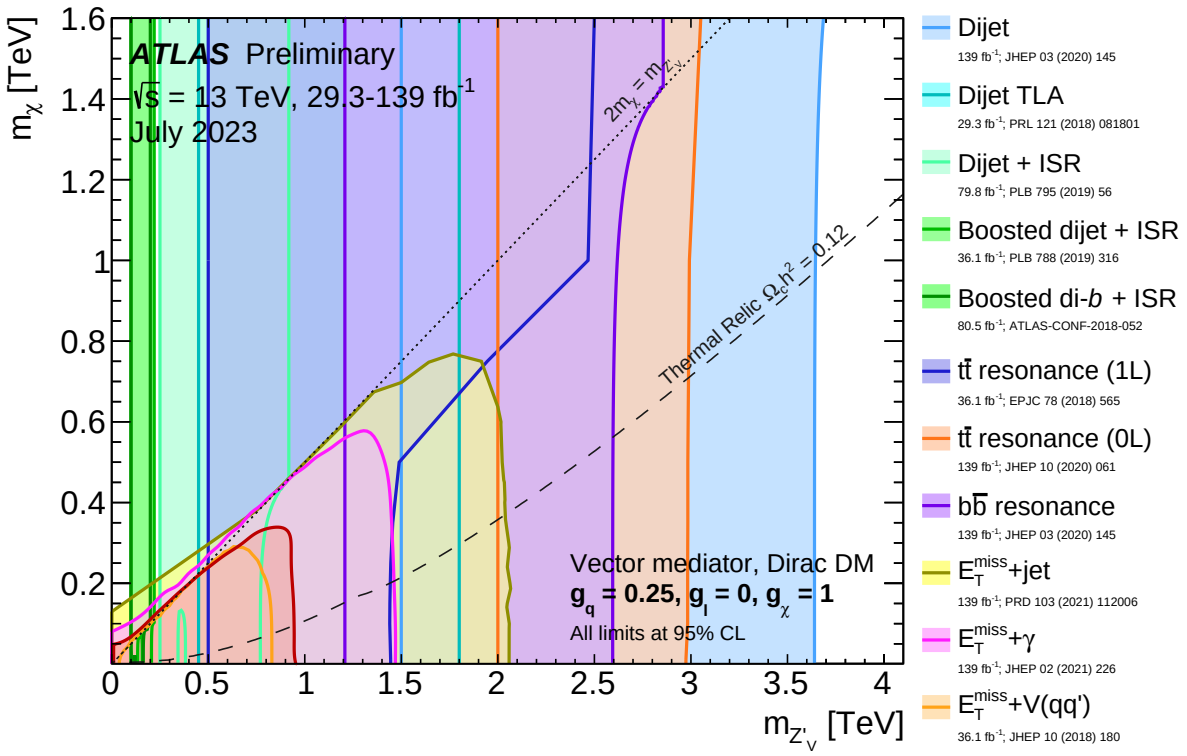

Figure 6: Regions in the (mediator-mass, DM-mass) plane excluded at 95% CL by dijet, dilepton and $E_{\mathrm{T}}^{\mathrm{miss}}+X$ searches, for leptophobic vector mediator simplified models. The exclusions are computed for a DM coupling $g_\chi = 1$, quark coupling $g_q = 0.25$, universal to all flavours, and no coupling to leptons. Dashed curves labelled "thermal relic" correspond to combinations of DM and mediator mass values that are consistent with a DM density of $\Omega h^2 = 0.12$ and a standard thermal history as computed in MadDM [7, 8]. Above the curve, annihilation processes described by the simplified model deplete Ωh^2 to below 0.12. The dotted line indicates the kinematic threshold where the mediator can decay on-shell into DM. The reinterpretation procedure for the TLA analysis follows the procedure recommended by ATLAS in Appendix A of Ref. [10], while the high-mass dijet and dijet+ISR analyses are reinterpreted following Ref. [11].

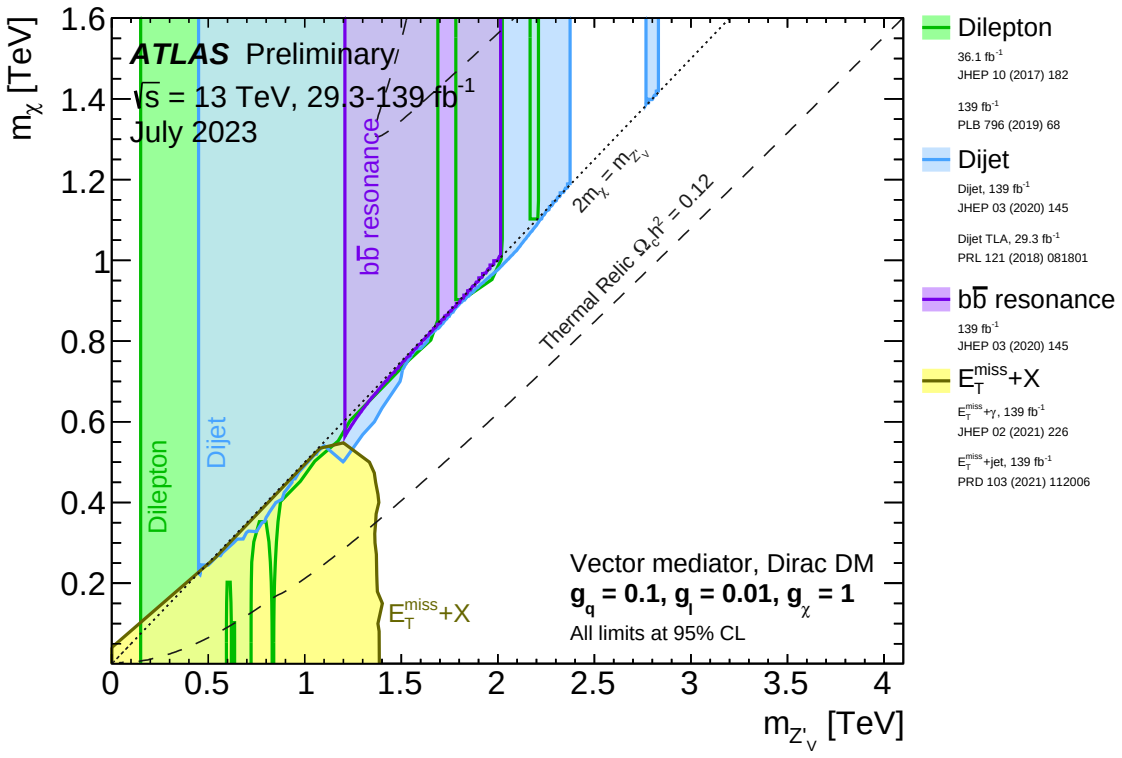

Figure 7: Regions in the (mediator-mass, DM-mass) plane excluded at 95% CL by dijet, dilepton and $E_{\mathrm{T}}^{\mathrm{miss}}+X$ searches, for leptophilic vector mediator simplified models. Each shaded region represents the union of the exclusion contours of the individual analyses listed in the legend, where more than one result contributes. The exclusions are computed for a DM coupling $g_\chi = 1$, quark coupling $g_q = 0.1$, and lepton coupling $g_l = 0.01$, in both cases universal to all flavours. Dashed curves labelled "thermal relic" correspond to combinations of DM and mediator mass values that are consistent with a DM density of $\Omega h^2 = 0.12$ and a standard thermal history as computed in MadDM [7, 8]. Between the two dashed curves, annihilation processes described by the simplified model deplete Ωh^2 to below 0.12. The dotted line indicates the kinematic threshold where the mediator can decay on-shell into DM.

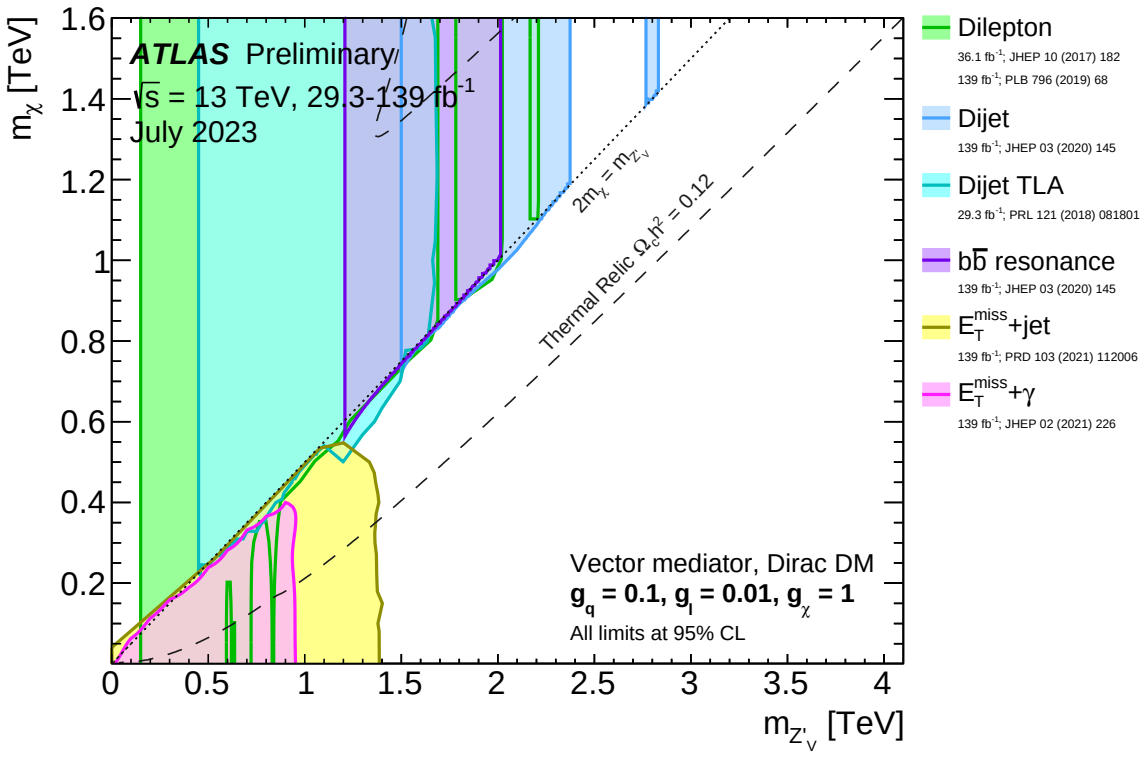

Figure 8: Regions in the (mediator-mass, DM-mass) plane excluded at 95% CL by dijet, dilepton and $E_{\mathrm{T}}^{\mathrm{miss}}+X$ searches, for leptophilic vector mediator simplified models. The exclusions are computed for a DM coupling $g_\chi = 1$, quark coupling $g_q = 0.1$, and lepton coupling $g_l = 0.01$, in both cases universal to all flavours. Dashed curves labelled "thermal relic" correspond to combinations of DM and mediator mass values that are consistent with a DM density of $\Omega h^2 = 0.12$ and a standard thermal history as computed in MadDM [7, 8]. Between the two dashed curves, annihilation processes described by the simplified model deplete Ωh^2 to below 0.12. The dotted line indicates the kinematic threshold where the mediator can decay on-shell into DM.

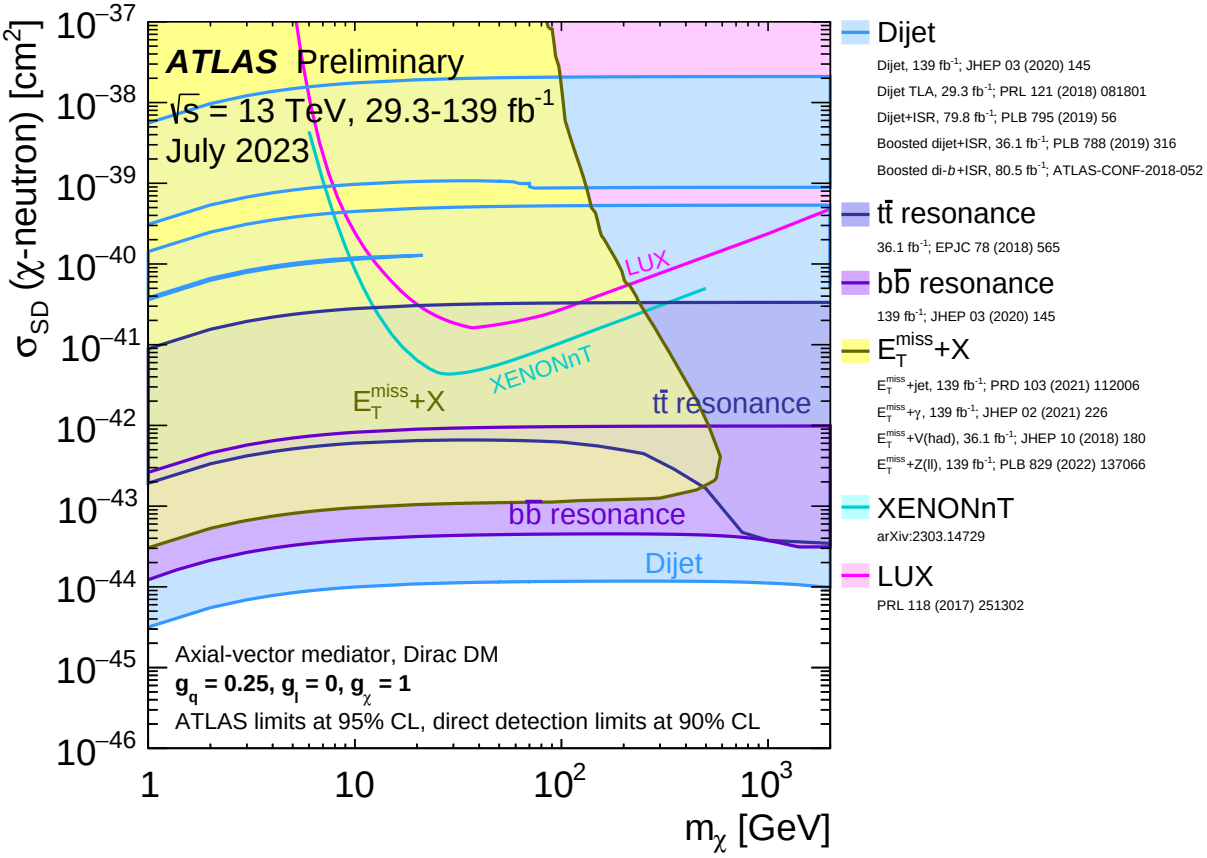

Figure 9: A comparison of the inferred limits with the constraints from direct-detection experiments on the spin-dependent WIMP–neutron cross-section in the context of the leptophobic axial-vector mediator simplified model. Each shaded region represents the union of the exclusion contours of the individual analyses listed in the legend, where more than one result contributes. The results from this analysis are compared with limits from direct-detection experiments. LHC limits are shown at 95% CL and direct-detection limits at 90% CL. The comparison is valid solely in the context of this model, assuming a mediator width fixed by the dark matter mass, a DM coupling $g_\chi = 1$, quark coupling $g_q = 0.25$, and no coupling to leptons. LHC searches and direct-detection experiments exclude only the shaded areas. Exclusions of smaller scattering cross-sections do not imply that larger scattering cross-sections are also excluded. The resonance and $E_{\mathrm{T}}^{\mathrm{miss}}+X$ exclusion regions represent the union of exclusions from all analyses of that type.

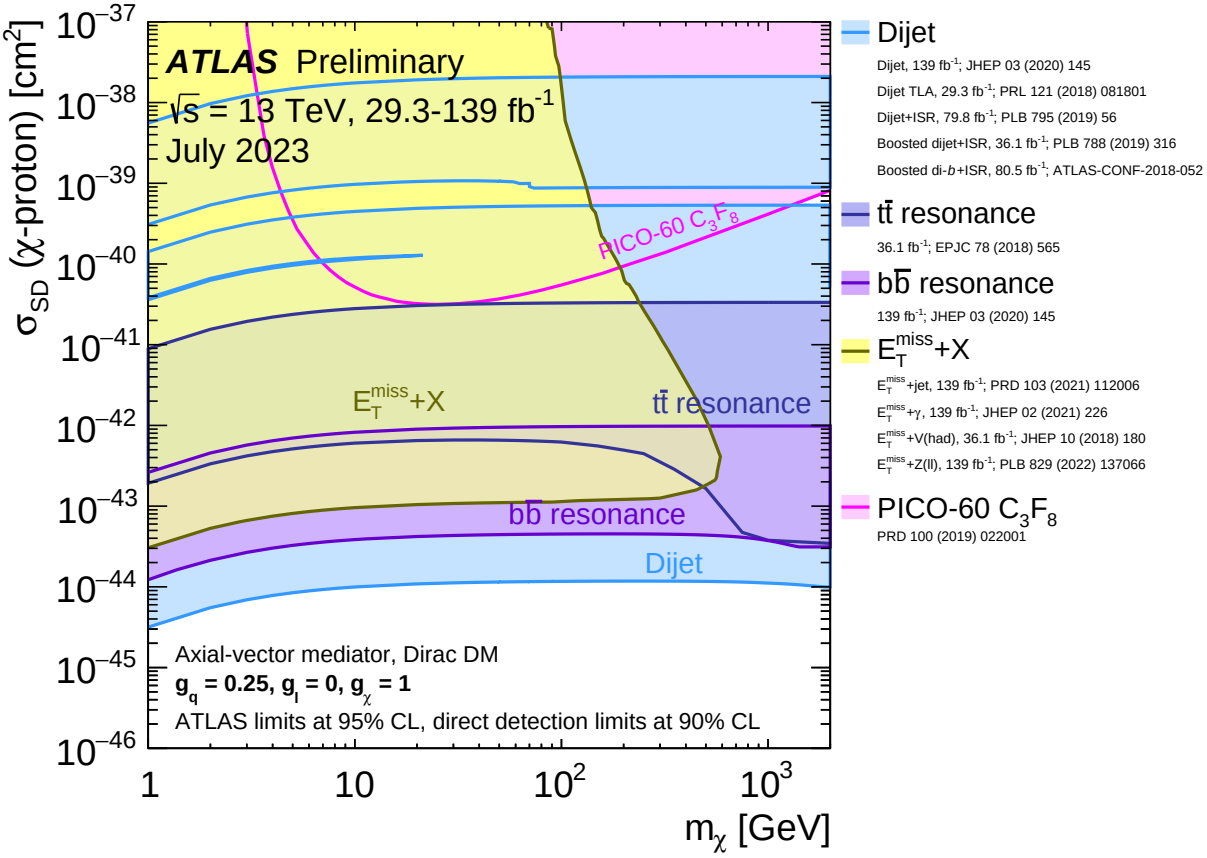

Figure 10: A comparison of the inferred limits with the constraints from direct-detection experiments on the spin-dependent WIMP–proton cross-section in the context of the leptophobic axial-vector mediator simplified model. Each shaded region represents the union of the exclusion contours of the individual analyses listed in the legend, where more than one result contributes. The results from this analysis are compared with limits from direct-detection experiments. LHC limits are shown at 95% CL and direct-detection limits at 90% CL. The comparison is valid solely in the context of this model, assuming a mediator width fixed by the dark matter mass, a DM coupling $g_\chi = 1$, quark coupling $g_q = 0.25$, and no coupling to leptons. LHC searches and direct-detection experiments exclude only the shaded areas. Exclusions of smaller scattering cross-sections do not imply that larger scattering cross-sections are also excluded. The resonance and $E_{\mathrm{T}}^{\mathrm{miss}}+X$ exclusion regions represent the union of exclusions from all analyses of that type.

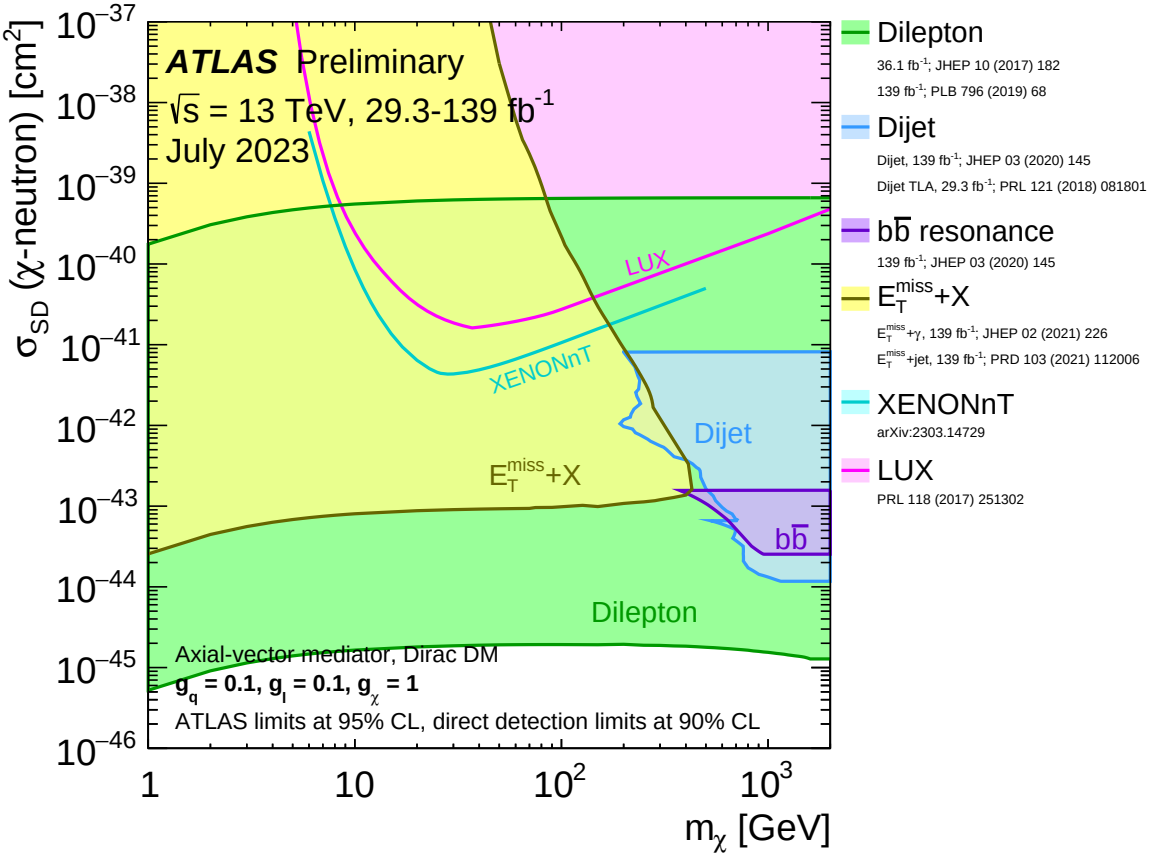

Figure 11: A comparison of the inferred limits with the constraints from direct-detection experiments on the spin-dependent WIMP–neutron scattering cross-section in the context of the leptophilic axial-vector mediator simplified model. Each shaded region represents the union of the exclusion contours of the individual analyses listed in the legend, where more than one result contributes. The results from this analysis are compared with limits from the direct-detection experiments. LHC limits are shown at 95% CL and direct-detection limits at 90% CL. The comparison is valid solely in the context of this model, assuming a mediator width fixed by the dark matter mass, a DM coupling $g_\chi = 1$, quark coupling $g_q = 0.1$, and lepton coupling $g_l = 0.1$. LHC searches and direct-detection experiments exclude only the shaded areas. Exclusions of smaller scattering cross-sections do not imply that larger scattering cross-sections are also excluded. The resonance and $E_{\mathrm{T}}^{\mathrm{miss}}+X$ exclusion region represents the union of exclusions from all analyses of that type.

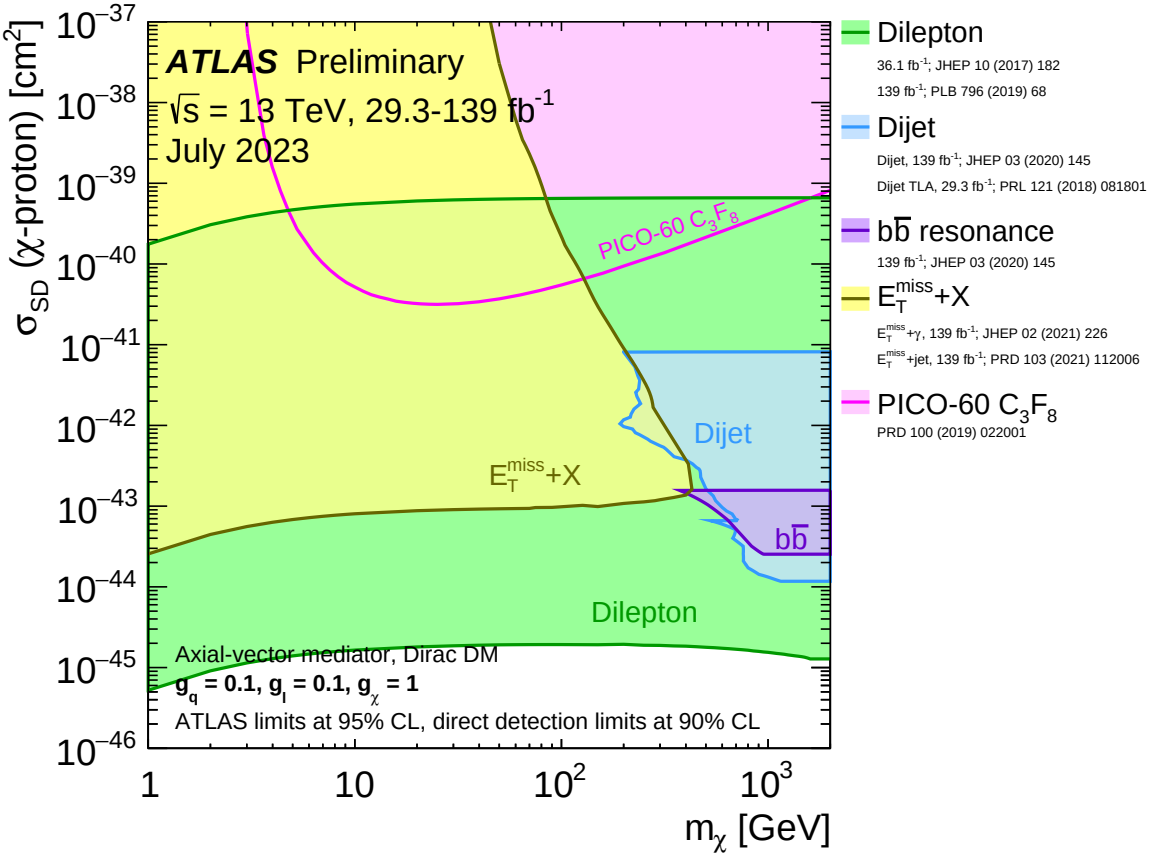

Figure 12: A comparison of the inferred limits with the constraints from direct-detection experiments on the spin-dependent WIMP–proton scattering cross-section in the context of the leptophilic axial-vector mediator simplified model. Each shaded region represents the union of the exclusion contours of the individual analyses listed in the legend, where more than one result contributes. The results from this analysis are compared with limits from the direct-detection experiments. LHC limits are shown at 95% CL and direct-detection limits at 90% CL. The comparison is valid solely in the context of this model, assuming a mediator width fixed by the dark matter mass, a DM coupling $g_\chi = 1$, quark coupling $g_q = 0.1$, and lepton coupling $g_l = 0.1$. LHC searches and direct-detection experiments exclude only the shaded areas. Exclusions of smaller scattering cross-sections do not imply that larger scattering cross-sections are also excluded. The resonance and $E_{\mathrm{T}}^{\mathrm{miss}}+X$ exclusion region represents the union of exclusions from all analyses of that type.

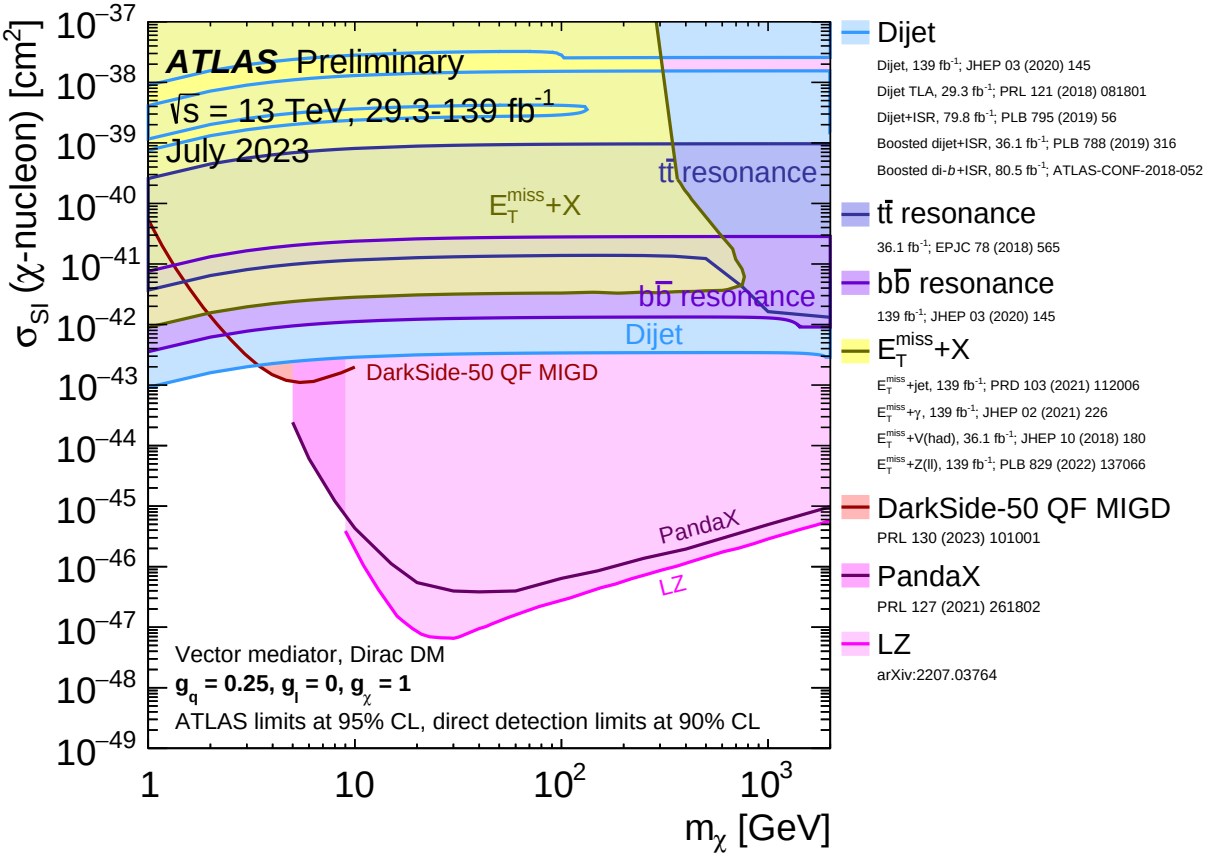

Figure 13: A comparison of the inferred limits with the constraints from direct-detection experiments on the spin-independent WIMP–nucleon scattering cross-section in the context of the leptophobic vector mediator simplified model. Each shaded region represents the union of the exclusion contours of the individual analyses listed in the legend, where more than one result contributes. The results from this analysis are compared with limits from the direct-detection experiments. LHC limits are shown at 95% CL and direct-detection limits at 90% CL. The comparison is valid solely in the context of this model, assuming a mediator width fixed by the dark matter mass, a DM coupling $g_\chi = 1$, quark coupling $g_q = 0.25$, and no coupling to leptons. LHC searches and direct-detection experiments exclude only the shaded areas. Exclusions of smaller scattering cross-sections do not imply that larger scattering cross-sections are also excluded. The resonance and $E_{\mathrm{T}}^{\mathrm{miss}}+X$ exclusion region represents the union of exclusions from all analyses of that type.

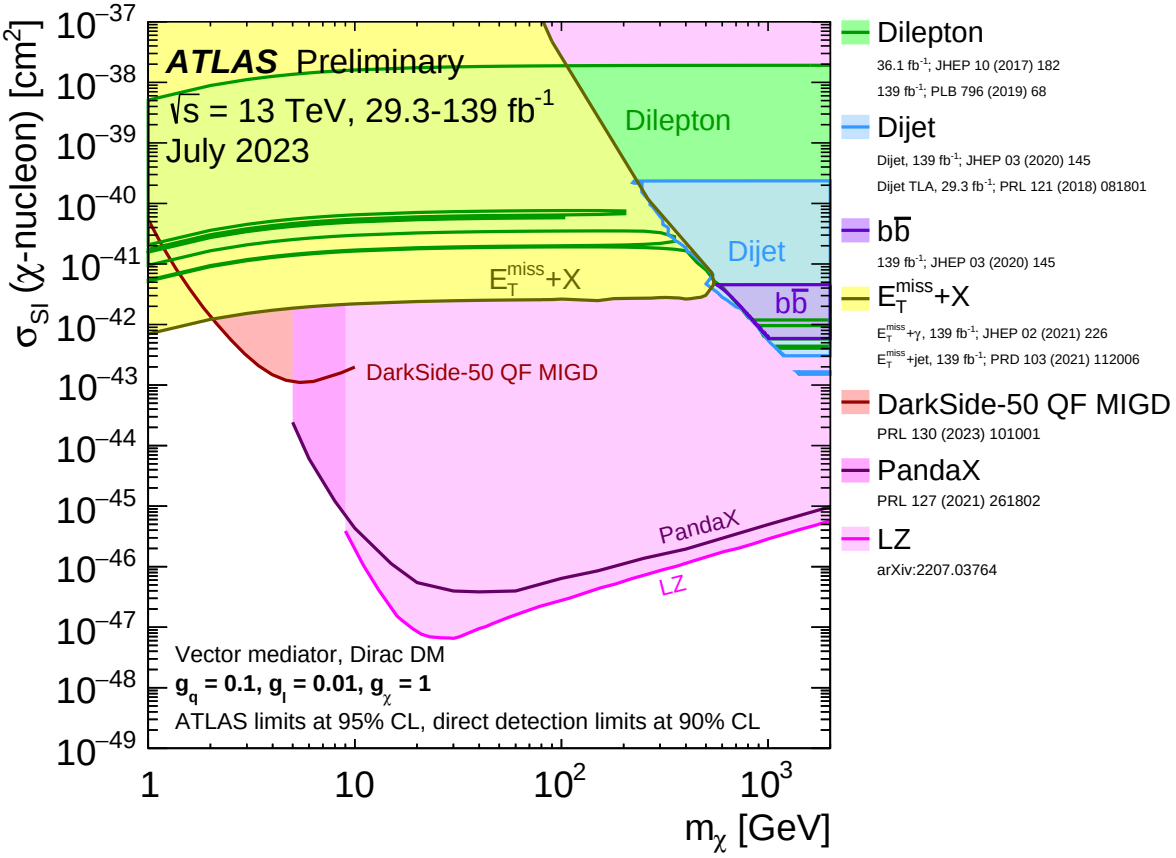

Figure 14: A comparison of the inferred limits with the constraints from direct-detection experiments on the spin-independent WIMP–nucleon scattering cross-section in the context of the leptophilic vector mediator simplified model. Each shaded region represents the union of the exclusion contours of the individual analyses listed in the legend, where more than one result contributes. The results from this analysis are compared with limits from the direct-detection experiments. LHC limits are shown at 95% CL and direct-detection limits at 90% CL. The comparison is valid solely in the context of this model, assuming a mediator width fixed by the dark matter mass, a DM coupling $g_\chi = 1$, quark coupling $g_q = 0.1$, and lepton coupling $g_l = 0.01$. LHC searches and direct-detection experiments exclude only the shaded areas. Exclusions of smaller scattering cross-sections do not imply that larger scattering cross-sections are also excluded. The resonance and $E_{\mathrm{T}}^{\mathrm{miss}}+X$ exclusion region represents the union of exclusions from all analyses of that type.

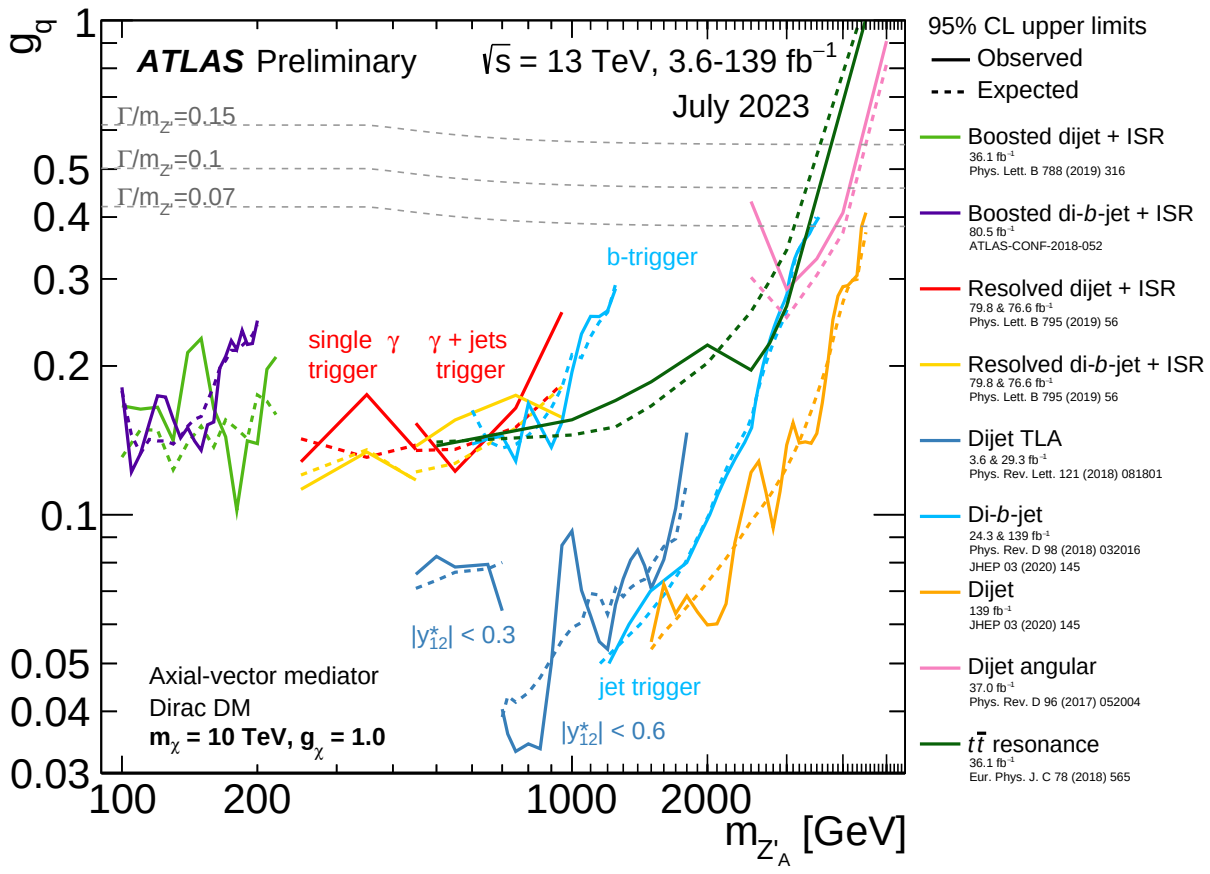

Figure 15: Hadronic resonance search contours for 95% CL upper limits on the coupling g_q as a function of the resonance mass $m_{Z'_A}$ for the leptophilic axial-vector mediator simplified model. The expected limits from each search are indicated by dotted lines. The TLA dijet analysis has two parts, employing different datasets with different selections in the rapidity difference y^* as indicated. The dijet+ISR (γ) analysis also has two parts, each using a different trigger strategy, and each further studied in inclusive and b-tagged channels. Two lines are also shown for the di-b-jet search. These are from separate analyses, one which used b-jet triggers and provides the limit at lower mass, and one which used inclusive jet triggers and provides the high mass limit. Coupling values above the solid lines are excluded, as long as the signals are narrow enough to be detected using these searches. The TLA dijet search with $|y^*| < 0.6$ is sensitive up to $\Gamma/m_{Z'} = 7\%$, the TLA dijet with $|y^*| < 0.3$ and dijet + ISR searches are sensitive up to $\Gamma/m_{Z'} = 10\%$, and the dijet and di-b-jet searches are sensitive up to $\Gamma/m_{Z'} = 15\%$. The dijet angular analysis is sensitive up to $\Gamma/m_{Z'} = 50\%$. No limitation in sensitivity arises from large width resonances in the $t\bar{t}$ resonance analysis. Benchmark width lines are indicated in the canvas. $\Gamma/m_{Z'} = 50\%$ lies beyond the canvas borders.

2.2 Spin-0 Mediators

The simplified model presented in this section introduce a Dirac fermion dark matter candidate, χ, and a new spin-zero particle, $\phi(a)$, which couples to Dark Matter and quarks with a new spin-zero scalar (pseudoscalar) particle [1, 12, 13]. The model assumes minimal flavour violation [14] and a Yukawa-like structure of the couplings of the new mediator to the SM particles, which include a common coupling g_q. The additional free parameters of the model are the masses of the Dark Matter m_χ, the mediator particles m_ϕ/m_a, and the coupling strength of the interactions between the mediator particle and Dark Matter particles g_χ.

Different implementations of the simplified model have been used for the interpretation of DM searches with different final states as follows:

***Implementation 1 – DM + bottom quarks*:** considers scalar and pseudoscalar mediators produced in association with a pair of bottom quarks (DMbb). The production cross-sections for these models were evaluated including NLO QCD corrections assuming SM Yukawa couplings to quarks, in a five-flavour scheme, following Ref. [15].

***Implementation 2 – DM + top quarks*:** considers scalar and pseudoscalar mediators produced in association with a pair of top quarks (DMtt) and, in addition, single top quark production referred as DMt. Both productions use *DMsimp* implementation [16]. Signal samples for DMtt are generated using a LO matrix element, with up to one extra parton using the MadGraph5_aMC@NLO [17] generator interfaced to Pythia and using the CKKW-L merging algorithm [18]. The top quark decay is simulated using MadSpin [19]. Signal cross sections for the DMtt process are calculated to NLO QCD accuracy using the same version of MadGraph, as suggested in Ref. [16]. Signal samples for dark matter associated production with a single top quark are generated using the same settings as the DMtt. No extra partons from the matrix element are generated in this case. DMt signal models are generated separately for tW and the tj processes. Each one is normalised to the LO cross section predicted by the model and then the samples are combined (added together).

***Implementation 3 – DM + jets*:** For the interpretation of the mono-jet final state, scalar and pseudoscalar signal samples were simulated in Powheg Box [20–22] using a simplified model implementation described in Ref. [23]. The DMS_tloop model was used for the production with s-channel spin-0 scalar and pseudoscalar mediator exchange with the full quark-loop calculation at LO [24].

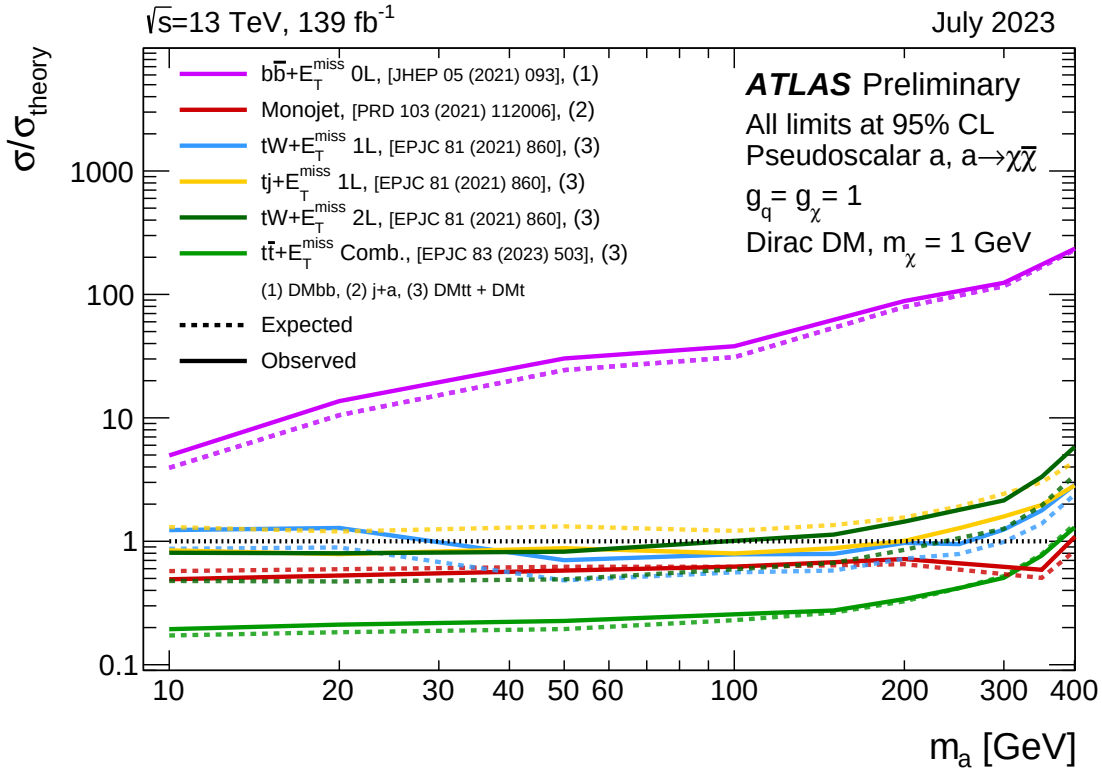

Figure 16: Exclusion limits for colour-neutral pseudoscalar mediator dark matter models [25] as a function of the mediator mass m_a for a dark matter mass m_χ of 1 GeV. The limits are calculated at 95% CL and are expressed in terms of the ratio of the excluded cross-section to the nominal cross-section for a coupling assumption of $g_q = g_\chi = 1$. The solid (dashed) lines show the observed (expected) exclusion limits for different analyses. The interpretation of the $b\bar{b}$+$E_{\mathrm{T}}^{\mathrm{miss}}$ 0L analysis, the tX+$E_{\mathrm{T}}^{\mathrm{miss}}$ analyses and the mono-jet analysis is made using the three implementations of the simplified spin-0 models described in the text.

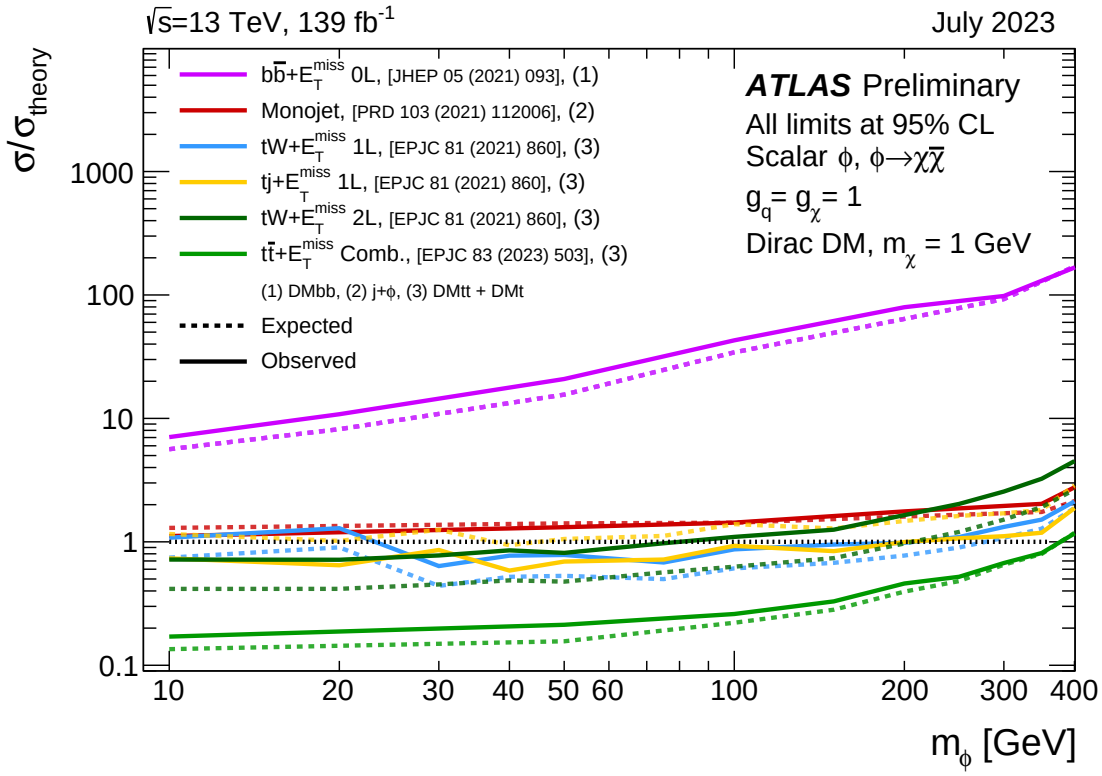

Figure 17: Exclusion limits for colour-neutral scalar mediator dark matter models [25] as a function of the mediator mass m_ϕ for a dark matter mass m_χ of 1 GeV. The limits are calculated at 95% CL and are expressed in terms of the ratio of the excluded cross-section to the nominal cross-section for a coupling assumption of $g_q = g_\chi = 1$. The solid (dashed) lines show the observed (expected) exclusion limits for different analyses. The interpretation of the $b\bar{b}$+$E_{\mathrm{T}}^{\mathrm{miss}}$ 0L analysis, the tX+$E_{\mathrm{T}}^{\mathrm{miss}}$ analyses and the mono-jet analysis is made using the three implementations of the simplified spin-0 models described in the text.

3 2HDM+a summary plots

This section provides the 2HDM+a [3] summary plots. All results have been released for the LHCP 2023 conference and submitted to Science Bulletin [26].

3.1 Overview of parameter scans

Table 1 summarises the parameter scans included, which have also been released in Ref. [26].

Table 1: Summary of the parameter settings for the different 2HDM+$a$benchmark scenarios.

Scenario		Fixed parameter values					Varied parameters
		$\sin\theta$	m_A [GeV]	m_a [GeV]	m_χ [GeV]	$\tan\beta$	
1	a	0.35	–	–	10	1.0	$(m_a\,, m_A)$
	b	0.70	–	–	10	1.0	
2	a	0.35	–	250	10	–	$(m_A, \tan\beta)$
	b	0.70	–	250	10	–	
3	a	0.35	600	–	10	–	$(m_a, \tan\beta)$
	b	0.70	600	–	10	–	
4	a	–	600	200	10	1.0	$\sin\theta$
	b	–	1000	350	10	1.0	
5		0.35	1000	400	–	1.0	m_χ
6		0.35	1200	–	–	1.0	(m_a, m_χ)

3.2 Results

3.2.1 Scenario 1: m_a – m_A planes

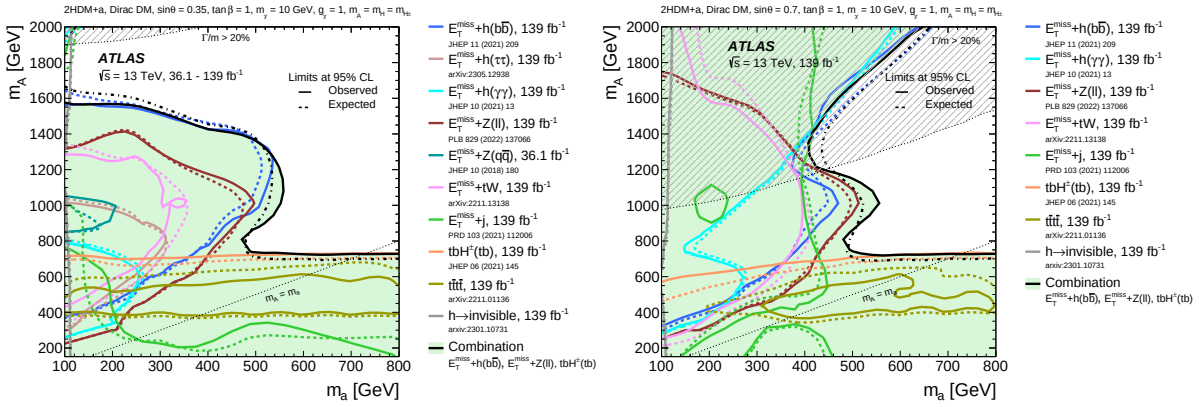

(a) (b)

Figure 18: Observed (solid lines) and expected (dashed lines) exclusion regions at 95% CL in the (m_a, m_A) plane assuming (a) $\sin\theta = 0.35$ (Scenario 1a) and (b) $\sin\theta = 0.7$ (Scenario 1b). The observed (solid lines) and expected (dashed lines) exclusion regions are shown for the statistical combination of the $E_{\mathrm{T}}^{\mathrm{miss}} + h(b\bar{b})$, $E_{\mathrm{T}}^{\mathrm{miss}} + Z(\ell^+\ell^-)$, and $H^{\pm}tb$ searches (filled area), for the three individual searches entering the combination, and additional individual searches. The dashed grey regions indicate the region where the width of any of the Higgs bosons exceeds 20% of its mass.

3.2.2 Scenario 2: m_A – $\tan\beta$ planes

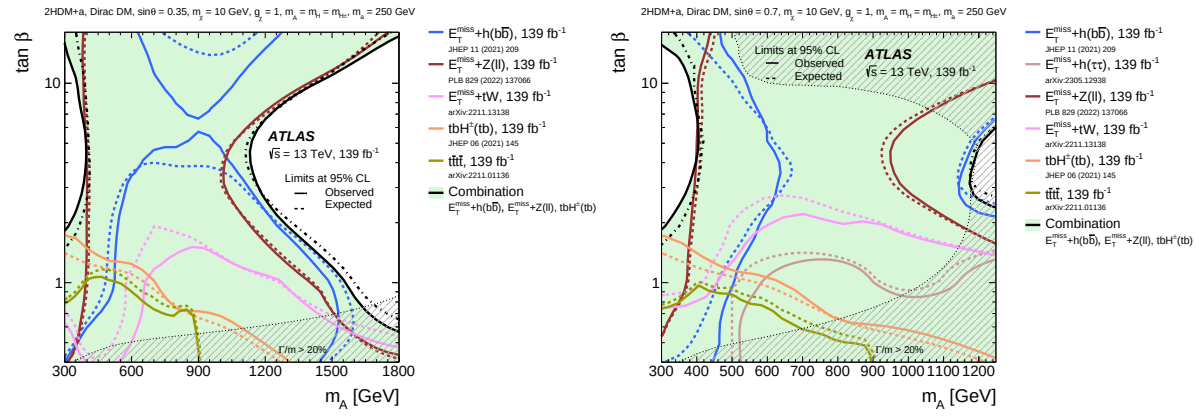

(a) (b)

Figure 19: Observed (solid lines and filled area) and expected (dashed lines) exclusion regions at 95% CL in the $(m_A\,, \tan\beta)$ plane assuming (a) $\sin\theta = 0.35$ (Scenario 2a) and (b) $\sin\theta = 0.7$ (Scenario 2b). The results are shown for several individual searches and the combination of the $E_{\mathrm{T}}^{\mathrm{miss}} + h(b\bar{b})$, $E_{\mathrm{T}}^{\mathrm{miss}} + Z(\ell^+\ell^-)$, and $H^{\pm}tb$ searches. The dashed grey regions indicate the region where the width of any of the Higgs bosons exceeds 20% of its mass.

3.2.3 Scenario 3: m_a – $\tan\beta$ planes

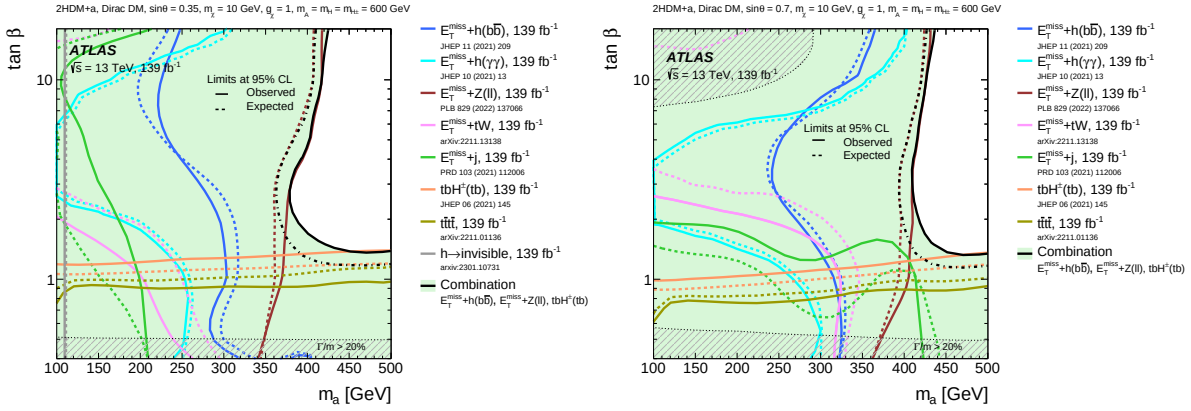

(a) (b)

Figure 20: Observed (solid lines and filled area) and expected (dashed lines) exclusion regions at 95% CL in the $(m_a, \tan\beta)$ plane assuming (a) $\sin\theta = 0.35$ (Scenario 3a) and (b) $\sin\theta = 0.7$ (Scenario 3b). The results are shown for several individual searches and the combination of the $E_{\mathrm{T}}^{\mathrm{miss}} + h(b\bar{b})$, $E_{\mathrm{T}}^{\mathrm{miss}} + Z(\ell^+\ell^-)$, and $H^{\pm}tb$ searches. The dashed grey regions indicate the region where the width of any of the Higgs bosons exceeds 20% of its mass.

3.2.4 Scenario 4: variation of $\sin\theta$

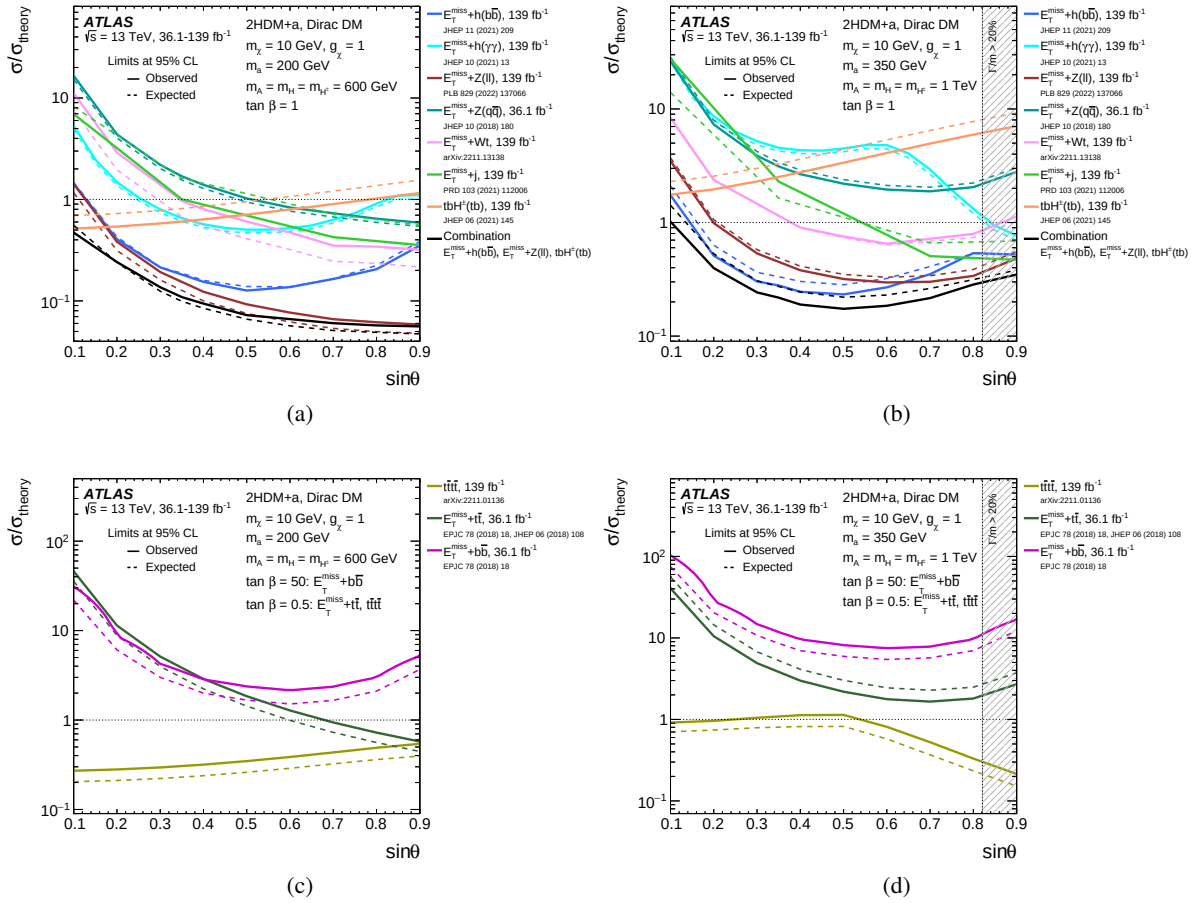

(a) (b) (c) (d)

Figure 21: Observed (solid lines) and expected (dashed lines) exclusion limits at 95% CL for the 2HDM+a as a function of $\sin\theta$. Results in the subfigures (a) and (b) are derived for the default value $\tan\beta = 1$ of Scenario 4, while those in subfigures (c) and (d) are for alternative values of $\tan\beta = 0.5$ or $\tan\beta = 50$. Subfigures (a) and (c) correspond to $m_A = 0.6$ TeV, $m_a = 200$ GeV (low-mass hypothesis), while (b) and (d) contain results for $m_A = 1.0$ TeV, $m_a = 350$ GeV (high-mass hypothesis). The results are shown for several individual searches and the combination of the $E_{\mathrm{T}}^{\mathrm{miss}} + h(b\bar{b})$, $E_{\mathrm{T}}^{\mathrm{miss}} + Z(\ell^+\ell^-)$, and $H^{\pm}tb$ searches. The dashed grey regions indicate the region where the width of any of the Higgs bosons exceeds 20% of its mass.

3.2.5 Scenario 5: variation of m_χ

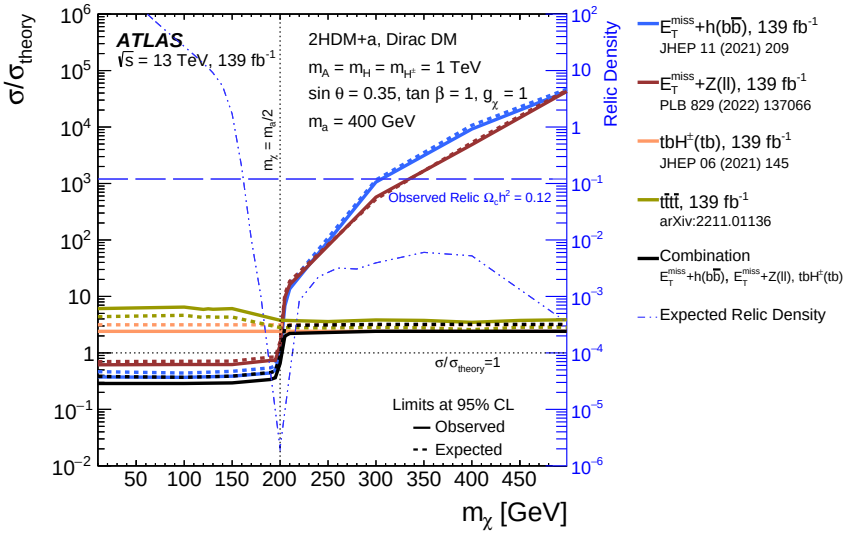

Figure 22: Observed (solid lines) and expected (dashed lines) exclusion limits for the 2HDM+a as a function of m_χ, following the parameter choices of $m_A = 1.0$ TeV, $m_a = 400$ GeV, $\tan\beta = 1.0$, and $\sin\theta = 0.35$ (Scenario 5). The limits are calculated at 95% CL and are expressed in terms of the ratio of the excluded cross-section to the nominal cross-section of the model. The results are shown for several individual searches and the combination of the $E_{\mathrm{T}}^{\mathrm{miss}} + Z(\ell^+\ell^-)$, $E_{\mathrm{T}}^{\mathrm{miss}} + h(b\bar{b})$, and $H^\pm tb$ searches. The relic density for each m_χ assumption, calculated with MadDM [7, 8], is superimposed in the plot (dashed line) and described by the right vertical axis. The valley at $m_\chi = 200$ GeV indicates the a-funnel region [3, 27, 28] where the predicted relic density is depleted by the resonant enhancement of the processes $\chi\bar{\chi} \to A/a \to$ SM.

3.2.6 Scenario 6: $m_a - m_\chi$ plane

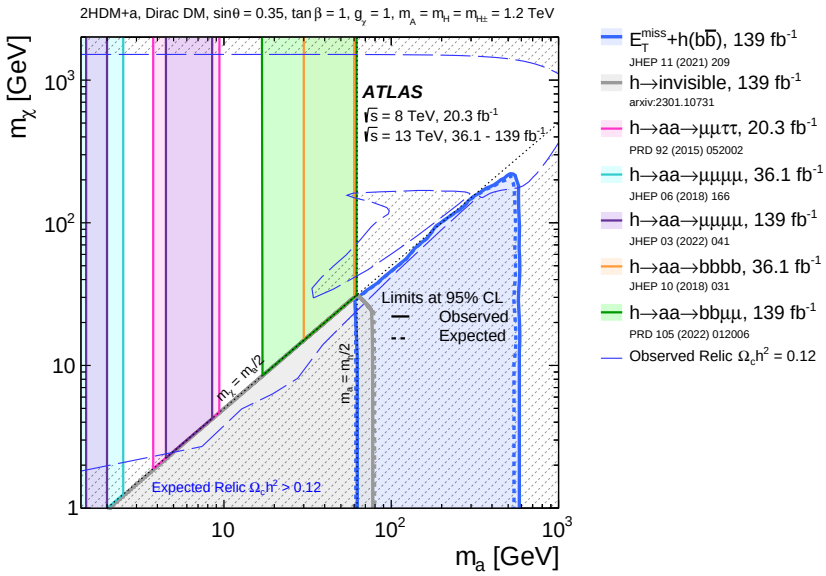

Figure 23: Observed (solid lines) and expected (dashed lines) exclusion regions at 95% CL in the (m_a , m_χ) plane following the parameter choices of $m_A = 1.2$ TeV, $\tan\beta = 1.0$, and $\sin\theta = 0.35$ (Scenario 6). The relic density contour for the case $\Omega_c h^2 = 0.12$, calculated with MadDM [7, 8], is superimposed in the plot (long-dashed line). The shaded regions mark parameter values for which the model predicts a relic density greater than the observed value $\Omega_c h^2 = 0.12$. The "island" around ($m_\chi \approx 100$ GeV, $m_a \approx 100$ GeV) corresponds to the resonant enhancement of the process $\chi\bar{\chi} \to ah \to$ SM, which depletes the relic density.

4 Higgs portal summary plot

This section provides a summary plot from the combination of searches for invisible decays of the Higgs boson. The upper limit on $B_{H\to inv}$ can be converted into a limit on the spin-independent scattering cross-section of a weakly interacting massive particle and a nucleon, to allow the comparison of the results with the ones from experiments based on different detector technologies. The translation is performed in the context of Higgs portal models [4, 5, 29] using an effective field theory framework for scalar, Majorana and vector DM. For vector DM the exclusion corresponding to a UV-complete model [30] is also provided. The result has already been published in Ref. [31].

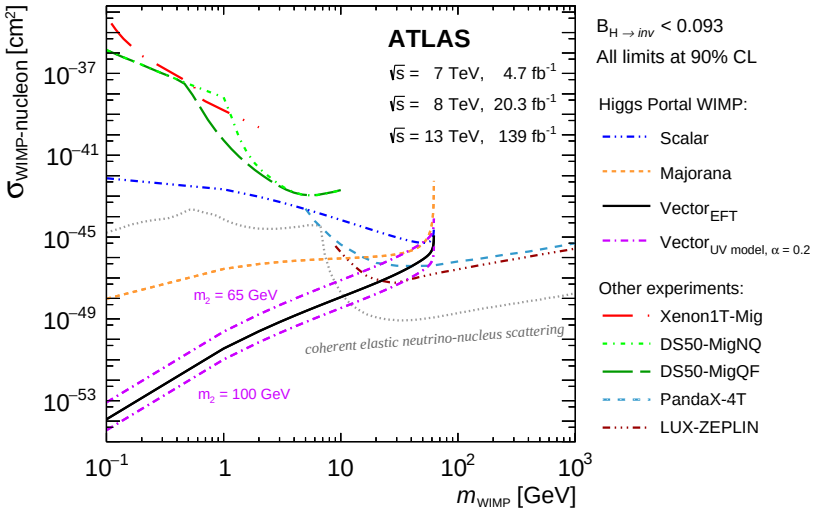

Figure 24: Upper limit at the 90% CL on the spin-independent WIMP-nucleon scattering cross-section as a function of the WIMP mass for direct detection experiments and the interpretation of the $H \to$ invisible combination result in the context of Higgs portal models considering scalar, Majorana and vector WIMP hypotheses [29]. For the vector case, results from a UV-complete model [30] are shown (pink curves) for two representative values for the mass of the predicted Dark Higgs particle (m_2) and a mixing angle α=0.2. The uncertainties from the nuclear form factor are smaller than the line thickness. Direct detection results are taken from Refs. [32–35]. The neutrino floor for coherent elastic neutrino-nucleus scattering (dotted gray line) is taken from Refs. [36, 37], which assume that germanium is the target over the whole WIMP mass range. The regions above the limit contours are excluded in the range shown in the plot.

5 Dark Higgs summary plot

This section provides a summary plot from analyses targetting the Dark Higgs Model [6]. This signal model provides a Majorana fermion dark matter candidate χ and two mediators: a vector boson Z' and a scalar dark Higgs boson s. The dark Higgs boson does not couple to SM particles, but can decay via mixing with the SM Higgs boson and hence has SM-like branching fractions as long as there are no new decay channels. The additional free parameters of this model are the masses of the Dark Matter m_χ, the mediator particles $m_{Z'}$ and m_s, the Z' coupling strength to quarks q_q and to DM g_χ, and the mixing angle θ between the SM and dark Higgs bosons.

5.1 Parameter scan

The summary plot shown in Fig. 25 corresponds to a benchmark with $g_q = 0.25$, $g_\chi = 1$, $\sin\theta = 0.01$, $m_\chi = 200$ GeV.

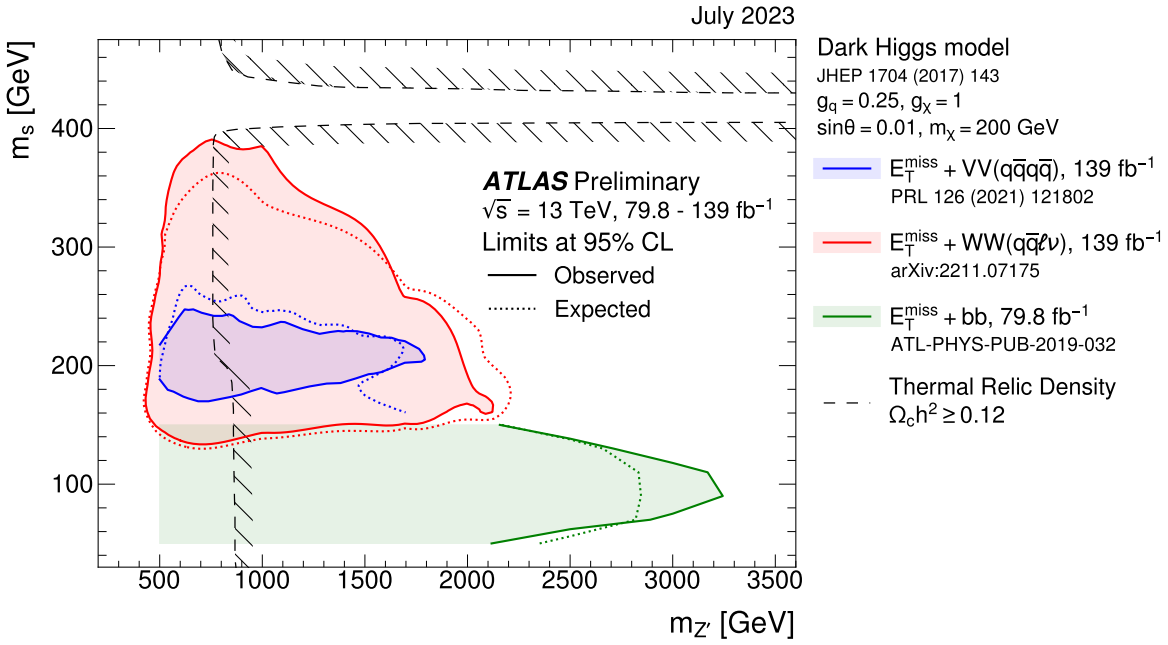

Figure 25: Observed (solid lines) and expected (dotted lines) exclusion limits at 95% CL for the Dark Higgs model in the $(m_{Z'}, m_s)$ plane under the assumption of $g_q = 0.25$, $g_\chi = 1$, $\sin\theta = 0.01$, $m_\chi = 200$ GeV. The open contours indicate regions of the mass plane not explored for that particular signature. The coloured areas are excluded. The dashed curve corresponds to the combinations of parameter values that are consistent with a DM density of $\Omega h^2 = 0.12$ and a standard thermal history, as computed in MadDM [7, 8], with the diagonal lines indicating which side corresponds to an overabundance of DM.

References

[1] D. Abercrombie et al., *Dark Matter benchmark models for early LHC Run-2 Searches: Report of the ATLAS/CMS Dark Matter Forum*, Phys. Dark Univ. **26** (2019) 100371, arXiv: 1507.00966 [hep-ex] (cit. on pp. 2, 18).

[2] J. Abdallah et al., *Simplified models for dark matter searches at the LHC*, Phys. Dark Univ. **9-10** (2015) 8, arXiv: 1506.03116 [hep-ph] (cit. on p. 2).

[3] T. Abe et al., *LHC Dark Matter Working Group: Next-generation spin-0 dark matter models*, Phys. Dark Univ. **27** (2020) 100351, arXiv: 1810.09420 [hep-ex] (cit. on pp. 2, 21, 25).

[4] A. Djouadi, A. Falkowski, Y. Mambrini and J. Quevillon, *Direct Detection of Higgs-Portal Dark Matter at the LHC*, Eur. Phys. J. C **73** (2013) 2455, arXiv: 1205.3169 [hep-ph] (cit. on pp. 2, 27).

[5] B. Patt and F. Wilczek, *Higgs-field portal into hidden sectors*, (2006), arXiv: hep-ph/0605188 (cit. on pp. 2, 27).

[6] M. Duerr et al., *Hunting the dark Higgs*, JHEP **04** (2017) 143, arXiv: 1701.08780 [hep-ph] (cit. on pp. 2, 27).

[7] A. Albert et al., *Recommendations of the LHC Dark Matter Working Group: Comparing LHC searches for heavy mediators of dark matter production in visible and invisible decay channels*, (2017), arXiv: 1703.05703 [hep-ex] (cit. on pp. 2–10, 25, 26, 28).

[8] M. Backovic, A. Martini, K. Kong, O. Mattelaer and G. Mohlabeng, *MadDM: New dark matter tool in the LHC era*, AIP Conf. Proc. **1743** (2016) 060001, arXiv: 1509.03683 [hep-ph] (cit. on pp. 3–10, 25, 26, 28).

[9] F. Kahlhoefer, K. Schmidt-Hoberg, T. Schwetz and S. Vogl, *Implications of unitarity and gauge invariance for simplified dark matter models*, JHEP **02** (2016) 016, arXiv: 1510.02110 [hep-ph] (cit. on pp. 3–6).

[10] ATLAS Collaboration, *Search for new phenomena in the dijet mass distribution using pp collision data at $\sqrt{s} = 8$ TeV with the ATLAS detector*, Phys. Rev. D **91** (2015) 052007, arXiv: 1407.1376 [hep-ex] (cit. on pp. 3, 4, 7, 8).

[11] CMS Collaboration, *Search for dijet resonances in proton–proton collisions at $\sqrt{s} = 13$ TeV and constraints on dark matter and other models*, Phys. Lett. B **769** (2017) 520, arXiv: 1611.03568 [hep-ex] (cit. on pp. 3, 4, 7, 8).

[12] M. R. Buckley, D. Feld and D. Goncalves, *Scalar simplified models for dark matter*, Phys. Rev. D **91** (2015), arXiv: 1410.6497 [hep-ph] (cit. on p. 18).

[13] U. Haisch and E. Re, *Simplified dark matter top-quark interactions at the LHC*, JHEP **06** (2015) 078, arXiv: 1503.00691 [hep-ph] (cit. on p. 18).

[14] ATLAS Collaboration, *Constraints on mediator-based dark matter and scalar dark energy models using $\sqrt{s} = 13$ TeV pp collision data collected by the ATLAS detector*, JHEP **05** (2019) 142, arXiv: 1903.01400 [hep-ex] (cit. on p. 18).

[15] Y. Afik et al., *DM+$b\bar{b}$ simulations with DMSimp: an update*, 2018, arXiv: 1811.08002 [hep-ex] (cit. on p. 18).

[16] M. Backovic et al., *Higher-order QCD predictions for dark matter production at the LHC in simplified models with s-channel mediators*, Eur. Phys. J. C **75** (2015) 482, arXiv: 1508.05327 [hep-ph] (cit. on p. 18).

[17] J. Alwall et al., *The automated computation of tree-level and next-to-leading order differential cross sections, and their matching to parton shower simulations*, JHEP **07** (2014) 079, arXiv: 1405.0301 [hep-ph] (cit. on p. 18).

[18] L. Lönnblad, *Correcting the Colour-Dipole Cascade Model with Fixed Order Matrix Elements*, JHEP **05** (2002) 046, arXiv: hep-ph/0112284 (cit. on p. 18).

[19] P. Artoisenet, R. Frederix, O. Mattelaer and R. Rietkerk, *Automatic spin-entangled decays of heavy resonances in Monte Carlo simulations*, JHEP **03** (2013) 015, arXiv: 1212.3460 [hep-ph] (cit. on p. 18).

[20] S. Alioli, P. Nason, C. Oleari and E. Re, *A general framework for implementing NLO calculations in shower Monte Carlo programs: the POWHEG BOX*, JHEP **06** (2010) 043, arXiv: 1002.2581 [hep-ph] (cit. on p. 18).

[21] S. Frixione, P. Nason and C. Oleari, *Matching NLO QCD computations with parton shower simulations: the POWHEG method*, JHEP **11** (2007) 070, arXiv: 0709.2092 [hep-ph] (cit. on p. 18).

[22] P. Nason, *A new method for combining NLO QCD with shower Monte Carlo algorithms*, JHEP **11** (2004) 040, arXiv: hep-ph/0409146 (cit. on p. 18).

[23] U. Haisch, F. Kahlhöfer and E. Re, *QCD effects in mono-jet searches for dark matter*, JHEP **12** (2013) 007, arXiv: 1310.4491 [hep-ph] (cit. on p. 18).

[24] U. Haisch and E. Re, *Simplified dark matter top-quark interactions at the LHC*, JHEP **06** (2015) 078, arXiv: 1503.00691 [hep-ph] (cit. on p. 18).

[25] D. Abercrombie et al., *Dark Matter benchmark models for early LHC Run-2 Searches: Report of the ATLAS/CMS Dark Matter Forum*, Phys. Dark Univ. **27** (2020) 100371, ed. by A. Boveia, C. Doglioni, S. Lowette, S. Malik and S. Mrenna, arXiv: 1507.00966 [hep-ex] (cit. on pp. 19, 20).

[26] G. Aad et al., *Combination and summary of ATLAS dark matter searches interpreted in a 2HDM with a pseudo-scalar mediator using 139 fb^{-1} of $\sqrt{s}$ = 13 TeV pp collision data*, (2023), arXiv: 2306.00641 [hep-ex] (cit. on p. 21).

[27] A. Djouadi, M. Drees and J.-L. Kneur, *Neutralino dark matter in mSUGRA: Reopening the light Higgs pole window*, Phys. Lett. B **624** (2005) 60, arXiv: hep-ph/0504090 [hep-ph] (cit. on p. 25).

[28] E. A. Bagnaschi et al., *Supersymmetric dark matter after LHC Run 1*, Eur. Phys. J. C **75** (2015) 500, arXiv: 1508.01173 [hep-ph] (cit. on p. 25).

[29] A. Djouadi, O. Lebedev, Y. Mambrini and J. Quevillon, *Implications of LHC searches for Higgs–portal dark matter*, Phys. Lett. B **709** (2012) 65, arXiv: 1112.3299 [hep-ph] (cit. on p. 27).

[30] G. Arcadi, A. Djouadi and M. Kado, *The Higgs-portal for vector dark matter and the effective field theory approach: A reappraisal*, Phys. Lett. B **805** (2020) 135427, arXiv: 2001.10750 [hep-ph] (cit. on p. 27).

[31] *Combination of searches for invisible decays of the Higgs boson using 139 fb−1 of proton-proton collision data at s=13 TeV collected with the ATLAS experiment*, Phys. Lett. B **842** (2023) 137963, arXiv: 2301.10731 [hep-ex] (cit. on p. 27).

[32] P. Agnes et al., *Search for Dark-Matter–Nucleon Interactions via Migdal Effect with DarkSide-50*, Phys. Rev. Lett. **130** (10 2023) 101001, arXiv: 1802.06994 (cit. on p. 27).

[33] Y. Meng et al., *Dark Matter Search Results from the PandaX-4T Commissioning Run*, Physical Review Letters **127** (2021), arXiv: 2107.13438 (cit. on p. 27).

[34] J. Aalbers et al., *First Dark Matter Search Results from the LUX-ZEPLIN (LZ) Experiment*, (2022), arXiv: 2207.03764 [hep-ex] (cit. on p. 27).

[35] E. Aprile et al., *Search for Light Dark Matter Interactions Enhanced by the Migdal Effect or Bremsstrahlung in XENON1T*, Phys. Rev. Lett. **123** (2019) 241803, arXiv: 1907.12771 [hep-ex] (cit. on p. 27).

[36] J. Billard, E. Figueroa-Feliciano and L. Strigari, *Implication of neutrino backgrounds on the reach of next generation dark matter direct detection experiments*, Physical Review D **89** (2014), arXiv: 1307.5458 [hep-ph] (cit. on p. 27).

[37] F. Ruppin, J. Billard, E. Figueroa-Feliciano and L. Strigari, *Complementarity of dark matter detectors in light of the neutrino background*, Physical Review D **90** (2014), arXiv: 1408.3581 (cit. on p. 27).